

Multi-Level Curvature-Based Parametrization and Model Updating Using a 3D Full-Field Response

Klemen Zaletelj^a, Domen Gorjup^a, Janko Slavič^{a,*}, Miha Boltežar^a

^a*University of Ljubljana, Faculty of Mechanical Engineering, Aškerčeva 6, 1000 Ljubljana, Slovenia*

Cite as:

*Klemen Zaletelj, Domen Gorjup, Janko Slavič and Miha Boltežar, Mechanical Systems and Signal Processing, Volume 187, 15 March 2023, 109927
<https://doi.org/10.1016/j.ymsp.2022.109927>*

Abstract

Model updating improves the correlation between the response of the real structure and the response of the finite-element (FE) model; however, the selection of the updating parameters (parametrization) is crucial for its success. Using full-field modal shapes, a large number of parameters can be updated, *e.g.*, the Young's moduli of all the finite elements; however, the structural response is not necessarily sensitive to an arbitrary parameter, making the optimization problem ill-conditioned. Additionally, the computation of the full sensitivity matrix is not feasible for relatively large FE models. Not all locations are equally important for model updating; at locations of the highest mechanical loads, more focus is required. In this research, the updating parameters are based on the curvature of the 3D full-field experimental shape, where locations with high curvature are associated with high sensitivity. The assumption is initially researched with the Euler-Bernoulli beam elements and second-order tetrahedrons. The proposed method is investigated on numerical and real experiments, where successful updating was confirmed. With the proposed parametrization and updating approach, a geometrically complex structure is parametrized and the parameters updated without significant user input, generalizing the model-updating procedure.

*Corresponding author

Email address: janko.slavic@fs.uni-lj.si (Janko Slavič)

Keywords: FE model updating, Interior Point Method, curvature-based parametrization, frequency-domain triangulation

1. Introduction

Finite-element (FE) model updating [1] minimizes the differences between the real structure and the FE model. The Marquardt approach is widely used to solve the non-linear least-squares minimization [2] of the cost function (a measure of the difference between the responses of the numerical model and the real structure). Weights have been applied to the measured data [1] and various regularization methods have been used to improve the conditioning of the inverse problem [3, 4]. Recently, Bayesian methods for model updating [5] have been heavily researched, and non-linear models were also updated [6, 7]. Because the cost function is usually smooth and convex near the optimal solution [8], the Interior Point Method (IPM) [9, 10] can be used to solve the minimization problem. The IPM successfully deals with the non-linear cost function as well as with the non-linear constraint functions of the updating parameters. Since the IPM is gradient-based, it is less computationally expensive than the global optimization algorithms [8].

Since the natural frequency is a global parameter, the modal shapes have to contribute the information about the local response behaviour. A spatially dense, full-field modal shape, in contrast to a sparse modal shape, provides the response information for the entire structure, making the localized parameter identification possible [11]. When updating a large number of parameters, the high spatial density of the response information ensures an over-determined optimization problem [11].

High-speed cameras have been used to capture the full-field, highly spatially dense response of the structure. One of the most widely used methods for displacement identification is the Digital Image Correlation (DIC) [12, 13] algorithm. For a DIC measurement, the surface of the object must have a unique visual pattern, *i.e.*, a speckle pattern, which is usually applied with a spray or a sticker [14] or is projected onto the surface [15]. Recently, the 3D DIC [16] technique with stroboscopic lighting was used by Su *et al.* [17] to characterize underwater propeller blades. Gorjup *et al.* [18] showed that, for a linear, time-invariant system, the 3D response can also be measured using a frequency-domain triangulation. Renaud *et al.* [19] used a single camera to reconstruct 3D shapes by projecting the FE modal shapes. In contrast,

a still camera was used by Javh *et al.* [20] and Gorjup *et al.* [21] to identify 2D [20] and 3D [21] full-field deflection shapes, respectively. Chen *et al.* [22] used a full-field measurement to identify the dynamics of a non-linear structure. Li *et al.* [23] used an adaptive filtering algorithm to enhance the signal power, decreasing the effect of the high noise level in the measurement. Javh *et al.* [24] proposed a hybrid method, a combination of the simplified optical flow method with a high-dynamic-range sensor to identify the modal shapes under the noise floor of the Frequency Response Function (FRF).

The full-field structural response has been seen as advantageous in identifying the localized anomalies on the structure; *e.g.*, Wang *et al.* [25] used Chebishev polynomials to compare the numerical and measured responses of the structure. Different full-field measurement methods were compared by Zanarini [26], *i.e.*, ESPI, SLDV and high-speed-camera measurements using 3D DIC. A sensitivity approach with full-field modal shapes obtained from high-speed-camera measurements was used by Cuadrado *et al.* [27] and location-specific weighting was introduced by Zaletelj *et al.* [11], to update a large number of localized parameters and identify the anomaly on the structure.

The updating parameters are typically chosen based on significant engineering insight. To avoid the parameter-selection process, Kim *et al.* [28] segmented the FEs based on the sensitivity of the response to the change of the FE property and improved the conditioning of the optimization problem. Shahverdi *et al.* [29] used a hierarchical dendrogram [30] to segment the columns of the sensitivity matrix and identify the parameters that have a similar effect; Bartilson *et al.* [3] also included modal shapes in the segment selection. Bartilson *et al.* [4] used the Singular Value Decomposition (SVD) algorithm to compute the reduced-order parametrization.

While the segmentation (the term clustering is used by some authors) of the finite elements has been addressed in previous research, the computation of the response sensitivity to each FE parameter was required, making the approach computationally expensive and not feasible for large FE models. Additionally, full-field response data were not used with the researched parametrizations. In this research, the parameter segments are determined for each experimental 3D full-field shape separately, based on the shape's curvature. Using the modal shapes, the updating is performed on multiple consecutive levels (starting with first modal shape), using a single parametrization on each level.

This manuscript is organized as follows. Section 2 presents the theoretical

background of the 3D-deflection-shape identification and the finite-element-model-updating method. Section 3 introduces multi-level parametrization, presents the justification for the curvature-based parametrization and lays out the updating algorithm. Sections 4 and 5 present the numerical and real experiment, respectively. The conclusions are drawn in Section 6.

2. Theoretical background

The prior knowledge about the 3D deflection shape's identification from a single high-speed camera using the frequency-domain triangulation [18] and the Interior Point Method for FE model updating [8] are discussed in this section.

2.1. Frequency-domain triangulation

To measure 3D deflection shapes using a single high-speed camera, the two-step frequency-domain triangulation method [18] is used. The first step in the shape-identification procedure is to measure the 2D deflection shape's images in multiple camera views. For Linear Time-Invariant (LTI) structures under stationary excitation, this can be achieved using a single camera by either moving the structure and keeping the camera stationary or changing the position of the camera around the structure. The camera's extrinsic parameters (positions and rotations relative to the structure) are reconstructed in a calibration using the test images [18]. For each of the multi-view measurements, the deflection shapes are computed by transforming the high-speed-image sequences of a structure under stationary broadband excitation into the frequency domain using Fourier Transform.

The second step of the procedure is the multi-view triangulation. Although the perspective camera projection is non-linear in Euclidean space, for a vibrating specimen exhibiting a small harmonic motion, the triangulation step can be performed in the frequency domain [18]. Using the multi-view frequency-domain deflection shape measurements, obtained in the first step of the procedure, together with the known positions of the observed points in the multiple views, spatial deflection shapes of the vibrating object are obtained using the linear triangulation algorithm [18]. The two steps of the frequency-domain triangulation procedure are outlined in Fig. 1.

In this research, the 3D response data were normalized to the measured excitation to form the FRFs [31]. Since the excitation profile was the same for all the camera views, one of the measured excitation signals was chosen

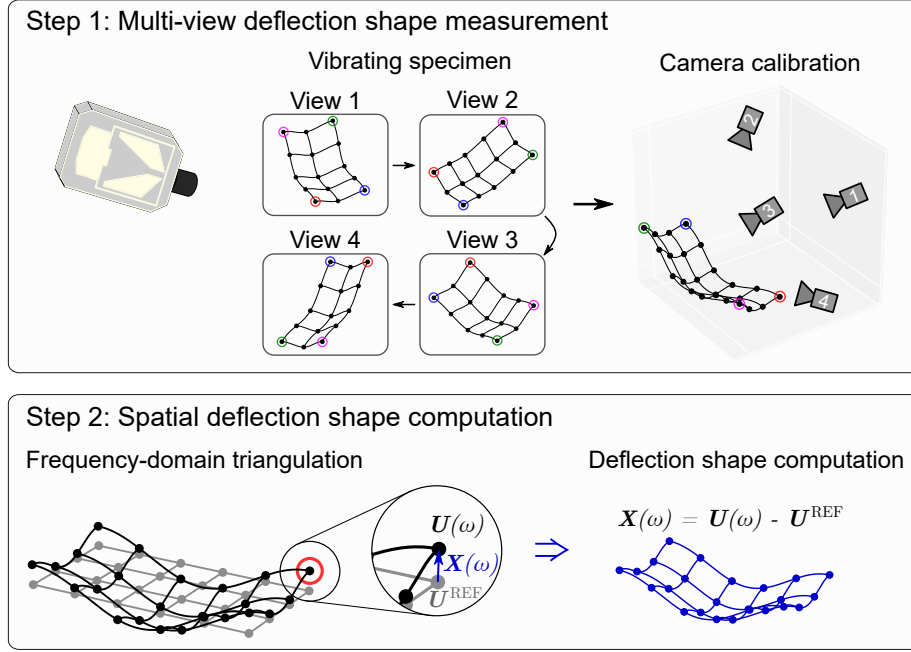


Figure 1: The frequency-domain triangulation procedure.

for the normalization. From the FRFs, the modal shapes were identified using a Python package pyEMA [32] and later used in the model-updating procedure.

2.2. Interior Point Method for model updating

To minimize the difference between the measured and the numerically computed values, *e.g.*, natural frequencies and modal shapes, the Interior Point Method [8] is used. The objective is to minimize a non-linear cost function $f(\boldsymbol{\theta})$ with respect to the updating parameters $\boldsymbol{\theta}$ that is subject to inequality constraints:

$$\begin{aligned} \min_{\boldsymbol{\theta}} \quad & f(\boldsymbol{\theta}) \\ \text{s.t.} \quad & g(\boldsymbol{\theta}) \leq \mathbf{0}, \end{aligned} \quad (1)$$

where $f: \mathbb{R}^r \rightarrow \mathbb{R}$ and $g: \mathbb{R}^r \rightarrow \mathbb{R}^q$. r is the number of updating parameters and q is the number of inequality constraints. The inequality constraints are defining the feasible region of the parameters, *e.g.*, a negative Young's modulus is physically not meaningful.

The cost function is defined as:

$$f(\boldsymbol{\theta}) = \|\hat{\boldsymbol{\lambda}} - \boldsymbol{\lambda}\|^2 + \|\hat{\boldsymbol{\phi}} - \boldsymbol{\phi}\|^2, \quad (2)$$

where $\hat{\boldsymbol{\lambda}} \in \mathbb{R}^m$ are the measured eigenvalues, $\boldsymbol{\lambda} \in \mathbb{R}^m$ are the numerical eigenvalues, $\hat{\boldsymbol{\phi}} \in \mathbb{R}^{m \times l}$ are the measured modal shapes and $\boldsymbol{\phi} \in \mathbb{R}^{m \times l}$ are the numerical modal shapes. m and l are the number of included eigenvalues/modal shapes and the number of locations in the modal shapes, respectively. $\|\cdot\|$ denotes the Euclidean norm. An issue of matching the modes from the measurement and numerical analysis arises when computing the cost following Eq. (2), since it is not necessary that all of the modal shapes are measured, making the simple ordering by natural frequency an inappropriate approach [1]. Additionally, the changes in the parameter values during the updating procedure can cause the shifting of shapes. This problem is generally addressed by implementing a Modal Assurance Criterion (MAC) [33] filter; the modes with the highest MAC value are paired. In this research, the eigenvalue similarity was also included in the mode-matching process by implementing the Modal Match Index (MMI) [34].

Usually, the modal shapes are compared using the MAC values [1], which is not ideal for updating the localized parameters, since it is, like the natural frequency, a global single index [35]. Instead, in Eq. (2), the modal shapes are compared location-by-location.

To minimize the cost function defined in Eq. (2), the inequality constraints $g(\boldsymbol{\theta})$ in Eq. (1) are rewritten as an equality constraint and a log-barrier term is added to prevent the constraint being violated [10]:

$$\begin{aligned} \min_{\boldsymbol{\theta}} \quad & f(\boldsymbol{\theta}) - \mu \sum_{i=1}^q \log(s_i) \\ \text{s.t.} \quad & g(\boldsymbol{\theta}) + \mathbf{s} = \mathbf{0}, \end{aligned} \quad (3)$$

where $\mathbf{s} \in \mathbb{R}^q$ is the vector of slack variables, $\mu \in \mathbb{R}$ is the barrier parameter and $\log(\cdot)$ denotes the natural logarithm. An additional constraint $\mathbf{s} \geq \mathbf{0}$ is implicitly included with the logarithmic term in Eq. (3) that prevents the slack variables approaching zero. The barrier parameter μ is iteratively reduced, as $\mu \rightarrow 0$, the minimizer of Eq. (3) approaches the minimizer of Eq. (1) [10].

From Eq. (3), a Lagrangian function to be minimized is defined [9]:

$$\mathcal{L}(\boldsymbol{\theta}, \mathbf{s}, \boldsymbol{\Gamma}) = f(\boldsymbol{\theta}) - \mu \sum_{i=1}^q \log(s_i) + \boldsymbol{\Gamma}^T \cdot (g(\boldsymbol{\theta}) + \mathbf{s}), \quad (4)$$

where $\mathcal{L} : \mathbb{R}^{r+q+q} \rightarrow \mathbb{R}$, $\boldsymbol{\Gamma} \in \mathbb{R}^q$ is the vector of Lagrange multipliers and dot (\cdot) denotes the matrix or vector multiplication. The Lagrangian, Eq. (4), can be minimized using an iterative Newtonian method. In each iteration j , the following system of equations must be solved:

$$\begin{bmatrix} \nabla_{\theta\theta}^2 \mathcal{L}_j & \mathbf{0} & \mathbf{A}_j^T \\ \mathbf{0} & \boldsymbol{\Sigma}_j & \mathbf{I} \\ \mathbf{A}_j & \mathbf{I} & \mathbf{0} \end{bmatrix} \cdot \begin{bmatrix} \mathbf{d}_\theta \\ \mathbf{d}_s \\ \mathbf{d}_\lambda \end{bmatrix} = - \begin{bmatrix} \nabla f(\boldsymbol{\theta}_j) + \mathbf{A}_j^T \cdot \boldsymbol{\Gamma}_j \\ \boldsymbol{\Gamma}_j - \mu \mathbf{S}_j^{-1} \cdot \mathbf{1} \\ g(\boldsymbol{\theta}_j) + \mathbf{s}_j \end{bmatrix}, \quad (5)$$

where $\nabla_{\theta\theta}^2 \mathcal{L}_j \in \mathbb{R}^{r \times r}$ is the Hessian of Eq. (4), $\nabla f(\boldsymbol{\theta}_j) \in \mathbb{R}^r$ is the gradient of $f(\boldsymbol{\theta}_j)$ and:

$$\begin{aligned} \mathbf{A}_j &= \nabla_{\theta} g(\boldsymbol{\theta}_j), & \mathbf{A}_j &\in \mathbb{R}^{q \times r} \\ \mathbf{S}_j &= \text{diag}(s_1, s_2, \dots), & \mathbf{S}_j &\in \mathbb{R}^{q \times q} \\ \boldsymbol{\Sigma}_j &= \mathbf{S}_j^{-1} \cdot \text{diag}(\Gamma_1, \Gamma_2, \dots), & \boldsymbol{\Sigma}_j &\in \mathbb{R}^{q \times q} \end{aligned} \quad (6)$$

An identity matrix is chosen as the Hessian of the Lagrangian [36] in the first iteration ($j = 1$), making the first step equivalent to the gradient-descent method. In the subsequent iterations, the Hessian is approximated by the Broyden-Fletcher-Goldfarb-Shanno (BFGS) formula, Eqs. (7-8) [36], making the procedure a quasi-Newtonian optimization.

$$\nabla_{\theta\theta}^2 \mathcal{L}_{j+1} = \nabla_{\theta\theta}^2 \mathcal{L}_j + \frac{\mathbf{q}_j \cdot \mathbf{q}_j^T}{\mathbf{q}_j^T \cdot \mathbf{d}_{x,j}} - \frac{\nabla_{\theta\theta}^2 \mathcal{L}_j \cdot \mathbf{d}_{\theta,j} \cdot \mathbf{d}_{\theta,j}^T \cdot \nabla_{\theta\theta}^2 \mathcal{L}_j^T}{\mathbf{d}_{\theta,j}^T \cdot \nabla_{\theta\theta}^2 \mathcal{L}_j \cdot \mathbf{d}_{\theta,j}}, \quad (7)$$

where:

$$\mathbf{q}_j = \nabla_{\theta} \mathcal{L}_{j+1} - \nabla_{\theta} \mathcal{L}_j \quad (8)$$

At every iteration, the new values of the parameters, slack variables and Lagrange multipliers are obtained as:

$$\begin{aligned} \boldsymbol{\theta}_{j+1} &= \boldsymbol{\theta}_j + \alpha_j \mathbf{d}_\theta \\ \mathbf{s}_{j+1} &= \mathbf{s}_j + \alpha_j \mathbf{d}_s \\ \boldsymbol{\lambda}_{j+1} &= \boldsymbol{\lambda}_j + \alpha_j \mathbf{d}_\lambda, \end{aligned} \quad (9)$$

where $\alpha_j \in (0, 1]$ determines the step size in the directions \mathbf{d}_θ , \mathbf{d}_s and \mathbf{d}_λ . α_j is computed based on a backtracking line search algorithm [10], ensuring a decrease in the cost function, Eq. (2), and preventing constraint violation.

The updating parameter θ is either a property of the numerical model (*e.g.*, density ρ) or a multiplier of this property. In this research, the parameters represent the property multipliers. The updated density ρ_{up} , for example, is then computed as:

$$\rho_{\text{up}} = \theta \rho_{\text{init}}. \quad (10)$$

3. Multi-level curvature-based parametrization and model updating

One of the major tasks in the model-updating procedure is the selection of the updating parameters (joint stiffness, density of a segment of the FE model, *etc.*) which requires significant engineering insight into a given problem [1]. Failing to select the appropriate updating parameters, the updated model fails to represent the real structure adequately [28].

In the case of updating a single model property, *e.g.*, the Young's modulus, the property of each element can be selected as an updating parameter, however, updating a property of every finite element separately usually fails to ensure adequate sensitivity of the structural response to all the updating parameters [29]. To improve the conditioning of the sensitivity matrix, the FE segments are determined [3, 4], which means the full sensitivity matrix must first be computed, a computationally expensive and, in cases of large FE models, not a feasible process. For a test case, a model with 2700 finite elements was used, where each evaluation of the numerical model took 9 seconds (on an HP ZBook i7). The evaluation of the sensitivities for all finite elements would take almost 7 hours.

An alternative approach is to correlate the areas of large strain with areas where mode shape is sensitive to parameter change. In addition, for bending and some torsional modes (in general, for modes that cause deflection in the normal direction to the surface) areas of high strain lead to areas of high surface curvature, see Sec. 3.1. However this is not necessarily true for axial and shear mode shapes. These generally have higher natural frequency and lower displacements, making the measurement with the high-speed camera a higher limiting factor compared to curvature detection. In this research, curvature-based segmentation is introduced. The segments are determined

by first identifying the curvature of a measured full-field modal shape and only the areas of the structure with a large curvature are segmented (Fig. 4). In contrast to existing methods, the presented method does not require numerous model evaluations; moreover, the parameterization of a single mode shape takes about 1 second (for 2300 points on an HP ZBook i7).

The curvature-based parametrization and the parametrization procedure are researched in the following sections.

3.1. Curvature-based parametrization of an Euler-Bernoulli beam

The relation of the curvature to the sensitivity of the natural frequency to the Young's modulus change can be seen in the Euler-Bernoulli free vibrating beam [37] governed by the differential equation:

$$\frac{\partial^2}{\partial x^2} \left(E(x) I \frac{\partial^2 \hat{w}(x)}{\partial x^2} \right) - \rho \omega^2 \hat{w}(x) = 0, \quad (11)$$

where:

$$w(x, t) = \hat{w}(x) e^{i\omega t} \quad (12)$$

$w(x, t)$ is the time-dependent deflection of the beam, $\hat{w}(x)$ is the amplitude of vibration, $E(x)$ is the Young's modulus dependent on the location x , ρ is the density, I is the area moment of inertia (considered a constant for all x), ω is the beam's natural frequency and $i = \sqrt{-1}$. Given the assumptions of the Euler-Bernoulli beam, the curvature of the beam is approximated as the second derivative of the deflection [37]:

$$\kappa(x) \approx \frac{\partial^2 \hat{w}(x)}{\partial x^2} \quad (13)$$

The relation between strain on the surface, ε , and the curvature, κ , is linear and can be expressed as [37]:

$$\varepsilon(x) = -z \frac{\partial^2 \hat{w}(x)}{\partial x^2} = -z \kappa(x) \quad (14)$$

where z is the coordinate of the beam surface.

If the curvature $\kappa(x)$ of a section on a beam $\mathbb{X} \in [x_1, x_2]$ is theoretically zero (in reality it is relatively small), from Eq. (13) it holds that:

$$\left. \frac{\partial^2 \hat{w}(x)}{\partial x^2} \right|_{\mathbb{X}} = 0 \quad (15)$$

Substituting Eq. (15) into Eq. (11), it is obvious that the change in Young’s modulus $E(x)$ in area \mathbb{X} does not impact the beam’s natural frequency ω . The sensitivity of ω to the Young’s modulus in area \mathbb{X} is therefore zero or, in reality, relatively small. In contrast, if the curvature is relatively large, so is the sensitivity.

The described relationship between the curvature and the sensitivity is presented for a numerical test case, where a beam with a *free-free* fixation was approximated using 50 Euler-Bernoulli finite elements and the curvatures of the modal shapes were computed. The beam had dimensions of 500 mm×30 mm×15 mm, with a density of 7400 kg/m³, Poisson’s ratio of 0.3 and Young’s modulus of 180 GPa. The sensitivities of the eigenvalues and modal shapes were computed by a numerical perturbation (0.1%) of the Young’s modulus for each element. As an example, the 4th modal shape and the absolute values of the curvature $\kappa(x)$ (13) are presented in Fig. 2a (both normalized to show the relative amplitude with respect to location). Fig. 2b shows the sensitivity of the eigenvalue and the sensitivity (averaged for all locations) of the modal shape to the change in the Young’s modulus at locations along the length of the beam.

Additionally, the curvature/sensitivity relationship is presented on a plate-like structure, approximated with second-order tetrahedrons. In Fig. 3, the areas of the plate with high curvature match the areas with high sensitivity.

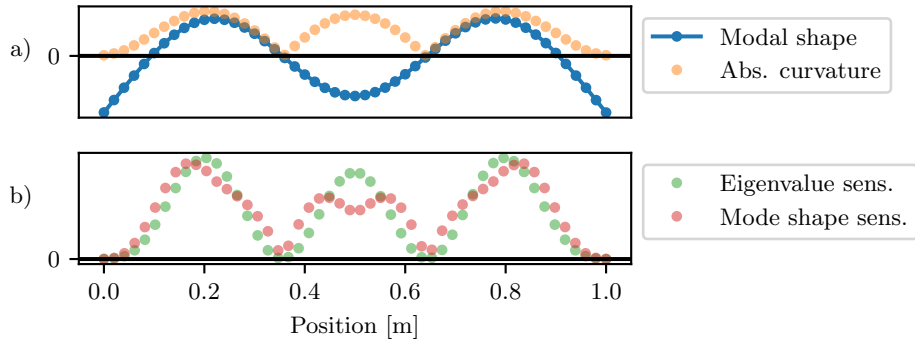


Figure 2: a) Normalized modal shape and curvature, and b) normalized eigenvalue and average modal shape sensitivity.

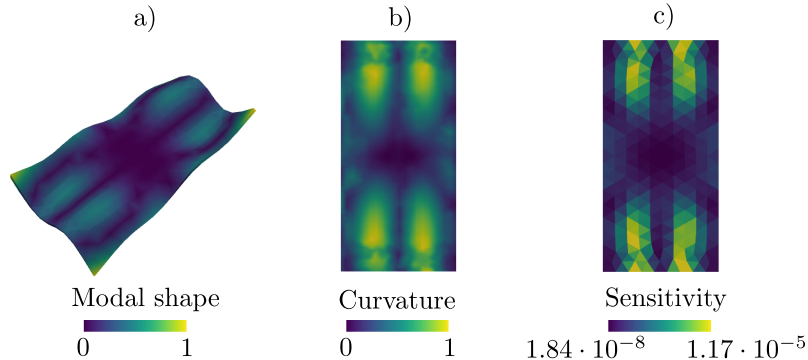


Figure 3: a) Modal shape of the plate, b) curvature of the upper surface of the plate and c) sensitivity of the eigenvalue to the change of Young’s modulus.

3.2. Generalization of curvature-based parameterization

The curvature at point $\mathbf{p}_i \in \mathbb{R}^3$ is computed as an estimation of the principal curvature, which is the maximum of the curvatures of the surface intersections with all the planes perpendicular to the tangent plane at a given point (normal curvatures) [38]. In this research, the principal curvature is estimated based on the modified umbrella method [39], originally used to estimate the Gaussian curvature. The details of the curvature estimation are presented in Appendix A.

To determine the segments associated with the updating parameters the areas with large curvature must be identified. A threshold value of curvature is selected and the areas with curvature larger than the threshold are segmented, see Fig. 4. Hierarchical clustering [30], with the average Euclidean distance of the element centers as a measure, is used for the segmentation. The areas with curvature values lower than the threshold value are viewed as a single segment and are given a single updating parameter.

The curvature-based parametrization is performed for each modal shape separately and the model is updated in multiple levels; in level i , the parameters are computed based on the curvature of the i -th modal shape. Parameters identified on level $i - 1$ are used as a starting point in level i . Modal shapes and eigenvalues from modes $[0, i]$ are included in the residual vector, all of the modal shapes are location-weighted by the curvature of the i -th modal shape.

The finite elements with a similar location and value of the updated pa-

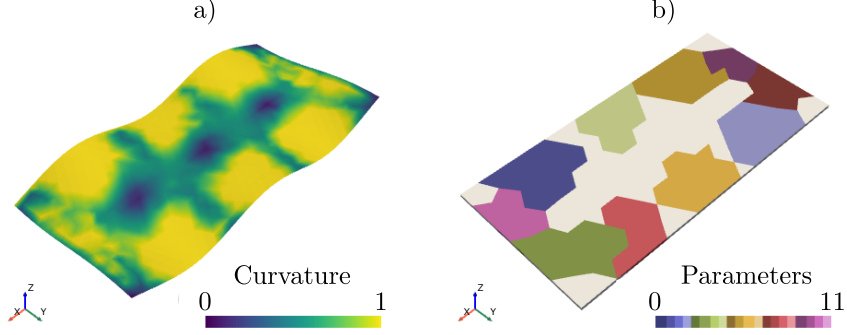


Figure 4: a) Curvature and b) example of parameter segments.

parameters from level $i - 1$ are clustered and combined with the segments from the curvature-based parametrization (Fig. 5) to ensure that the initial parameter values within a segment have similar values. Hierarchical clustering [30], with the average Euclidean distance as a measure, is used; the FE locations and parameter values are equally weighted:

$$\mathbf{D} = \begin{bmatrix} x_0 & y_0 & z_0 & E(x_0, y_0, z_0) \\ x_1 & y_1 & z_1 & E(x_1, y_1, z_1) \\ \vdots & \vdots & \vdots & \vdots \\ x_{n_{\text{el}}} & y_{n_{\text{el}}} & z_{n_{\text{el}}} & E(x_{n_{\text{el}}}, y_{n_{\text{el}}}, z_{n_{\text{el}}}) \end{bmatrix} \cdot \begin{bmatrix} w_{\text{loc}} \\ w_{\text{loc}} \\ w_{\text{loc}} \\ w_{\text{par}} \end{bmatrix}, \quad (16)$$

where w_{loc} and w_{par} are scalar weights, ensuring equal weighting of the location and parameter values:

$$w_{\text{loc}} = \frac{1}{\sqrt{\sum_{k=0}^{n_{\text{el}}} (x_k^2 + y_k^2 + z_k^2)}} \quad (17)$$

$$w_{\text{par}} = \frac{1}{\sqrt{\sum_{k=0}^{n_{\text{el}}} E(x_k, y_k, z_k)^2}} \quad (18)$$

The coordinates x_k , y_k and z_k are determined as average values of the nodal coordinates of the k -th element, and n_{el} is the number of elements in the FE model.

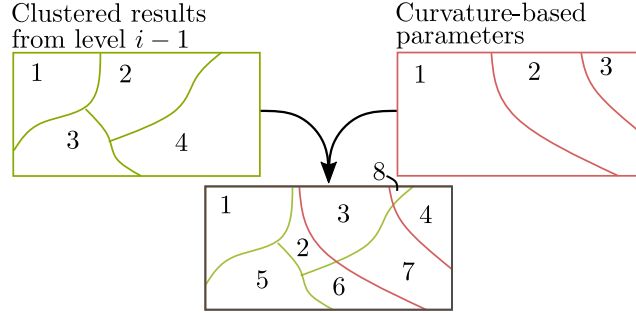


Figure 5: Combining curvature-based parameters and the clustered parameters from level $i-1$.

3.3. The multi-level curvature-based model-updating algorithm

The multi-level curvature-based model-updating procedure has the following steps:

1. Prepare experimental data.
2. Prepare numerical model:
 - (a) Define the FE mesh.
 - (b) Align the numerical model with the experimental locations (Appendix B).
 - (c) Define the initial parameter values.
3. Curvature-based parametrization (Sec. 3.2):
 - (a) Compute curvature of modal shapes.
 - (b) Determine threshold curvature and select areas with large curvature.
 - (c) Compute the segments associated with the updating parameters.
4. Location matching - compute the approximation of the measured modal shapes at nodes of the finite-element model Appendix B).
5. Start the iteration over the measured modal shapes ($i = 0$):
 - (a) Match numerical modes to the measured mode.
 - (b) If $i \neq 0$, cluster similar parameter values, Eq. (16).
 - (c) If $i \neq 0$, combine parametrizations from step 3. and step 5.(b), see Fig. 5.
 - (d) Use the Interior Point Method to identify the parameters (Sec. 2.2) for each segment.
 - (e) Update the FE model's properties of each segment by multiplying them by the identified parameter, Eq. (10).

(f) Increment $i = i + 1$ and repeat from step 5.(a).

The iteration starts with the mode at the lowest natural frequency since the modal shapes at lower frequencies are better related to the global response of the structure and are also related to larger amplitudes. With this approach, the global behaviour of the structure is corrected first, after which the local anomalies are addressed. The identified parameters from the last iteration i are the result of the model-updating procedure.

4. Numerical experiment

A numerical experiment where the true parameter values are known was conducted to test the proposed parametrization and updating method. In this section the data acquired by the numerical experiment are referred to as the experimental data.

A numerical model of a 3-plane cubic shell with three orthogonal sides of size 120 mm \times 120 mm (Fig. 6a) was used to numerically generate the data for the experimental model. A finite-element mesh with 14 419 second-order tetrahedrons was generated (Fig. 6b). The material properties were assigned to the finite elements. The material density ρ was 7850 kg/m³, its Young's modulus E was 200 GPa and its Poisson's ratio ν was 0.3. The Young's modulus was locally reduced to 80 GPa, as marked in Fig. 7a.

The 3D finite elements (tetrahedrons) are used in the numerical and real experiments in this research since they enable a rapid FE model preparation without extensive 3D-model simplifications. Membrane, plate or shell elements can also be used, depending on the structure type and user insight/preference.

The eigenvalues and modal shapes were identified for the experimental model; however, first seven modal modes were included in the experimental data to simulate a common real-measurement issue of unmeasured modes. Because no damping was included, the modal shapes were strictly real.

To simulate the noisy measurements, a normally distributed noise was added to the modal shapes:

$$\hat{\phi} = \phi + \Delta, \quad (19)$$

where $\phi \in \mathbb{R}^{l_e}$ is the noise-free modal shape, $\hat{\phi} \in \mathbb{R}^{l_e}$ is the noisy modal shape and $\Delta \in \mathbb{R}^{l_e}$ are samples of zero-mean normal distribution with the standard deviation $\sigma = 0.15 \bar{\phi}$, where $\bar{\phi}$ is the average of the modal shape. The added

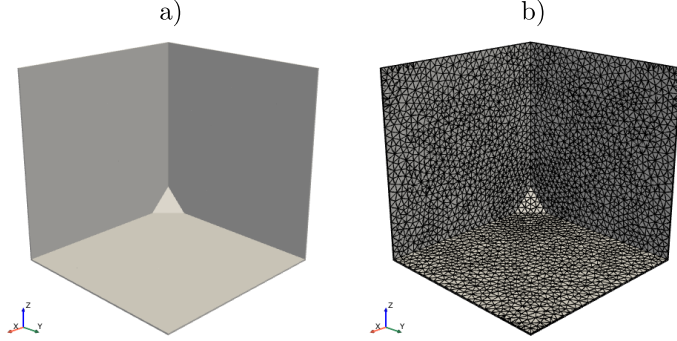


Figure 6: a) Numerical model for experiment simulation and b) the finite-element mesh with 14 419 elements.

noise is relatively high and corresponds to the one observed in high-speed-camera measurements. Similarly, the noise was added to the eigenvalues:

$$\hat{\lambda} = \lambda + \Delta, \quad (20)$$

where $\lambda \in \mathbb{R}$ is the noise-free eigenvalue, $\hat{\lambda} \in \mathbb{R}$ is the eigenvalue with noise and $\Delta \in \mathbb{R}$ is a sample of zero-mean normal distribution with $\sigma = 0.03 \lambda$.

The numerical model to be updated was similar to the experimental model (Fig. 6a); however, the number of elements was 4755 (as opposed to 14 419 for the simulated high-spatial density measurement with the high-speed camera). All the elements were given the same initial Young's modulus E of 190 GPa; density ρ and Poisson's ratio ν were assumed to be known and had values of 7850 kg/m³ and 0.3, respectively.

The updating procedure was carried out as described in Sec. 3.3. The true values of the Young's moduli are compared with the updated Young's moduli in Fig. 7. It is clear from Fig. 7 that the region with the lowered Young's modulus was identified. The error of the updated Young's modulus $\mathbf{E}_{\text{up}} \in \mathbb{R}^{n_n}$ with respect to the true values $\mathbf{E}_{\text{true}} \in \mathbb{R}^{n_e}$ was computed:

$$\mathbf{err} = \frac{(\mathbf{E}_{\text{true,appr.}} - \mathbf{E}_{\text{up}})^{\text{abs}}}{\mathbf{E}_{\text{true,appr.}}} \cdot 100\%, \quad (21)$$

where $\mathbf{E}_{\text{true,appr.}} \in \mathbb{R}^{n_n}$ are the approximated values of \mathbf{E}_{true} at the locations of \mathbf{E}_{up} , a necessary step caused by non-identical FE meshes. $(\cdot)^{\text{abs}}$ denotes

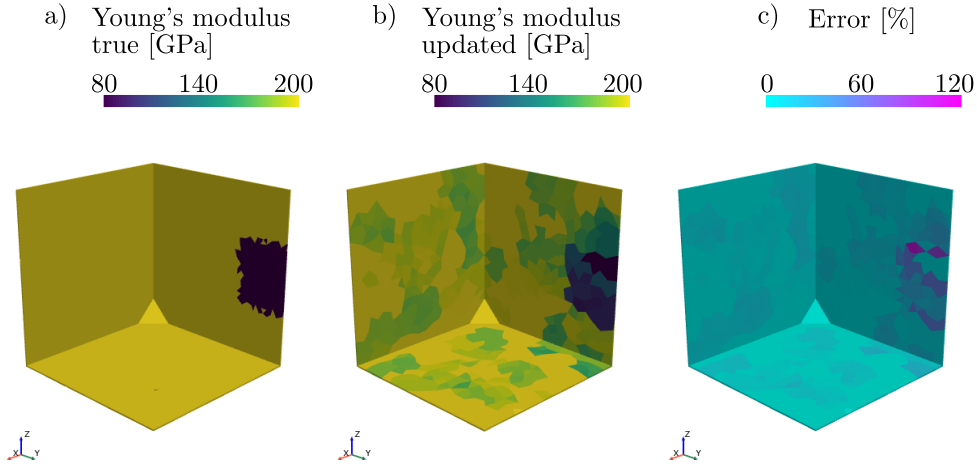


Figure 7: a) True Young's modulus values, b) updated Young's modulus values and c) the error in parameter identification.

taking the element-wise absolute value. The average of *err* was computed to be 5 %; the largest error (120 % in one of the elements) appeared at the edges of the area with the lowered stiffness. This was caused by the discrepancy of the mesh; the elements were not lined-up accurately and an approximation was used to compare the Young's moduli.

Figs. 8a and 8b show the MAC matrices before and after updating, it is obvious that the updated numerical model represents the experimental modal shapes significantly better than the initial model. It can also be seen from Fig. 8b that the matching modes are not on the diagonal but are shifted, indicating the numerical modes that were not measured. The MAC values of the matching modes are presented in Fig 8c, it is clear that all the updated MAC values are nearly close to unity; the minimal MAC value for the updated model is 0.98, while for the initial model it is 0.49, the average value of MAC for updated model is 0.994 and for the initial model it is 0.81. The MAC values significantly increased even for the modes that were not included in the updating procedure. In addition to the MAC values, the comparison of eigenvalues in Fig. 9, also shows that the updated numerical model represents the experimental model well; the eigenvalues from the updated model are closer to the experimental values and, similar to the MAC values, the eigenvalues that were not included in the updating procedure also approached the experimental values; the average error before

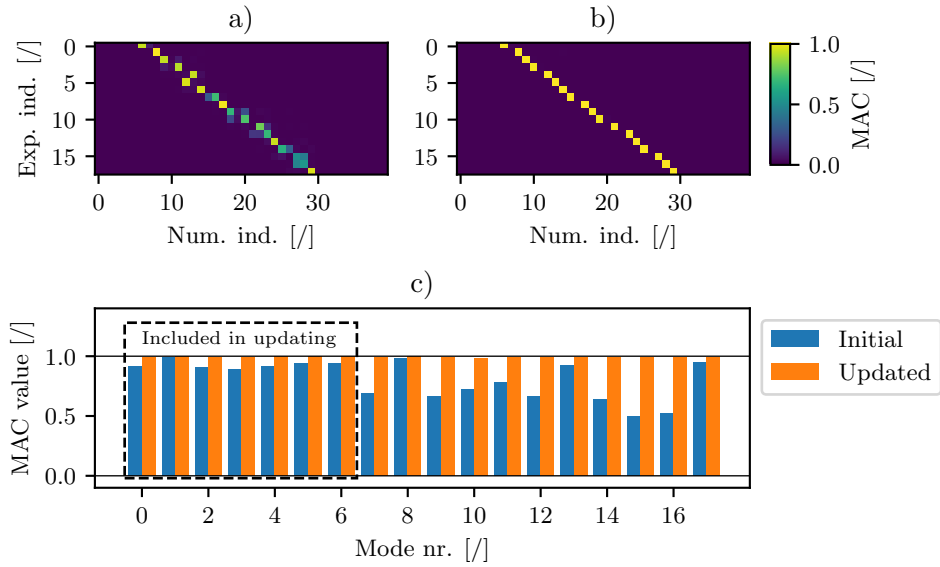


Figure 8: a) MAC matrix with initial Young's modulus values, b) MAC matrix with updated Young's modulus values and c) comparison of the MAC values of the matching modes.

the updating was 1% and after updating it was 0.1%.

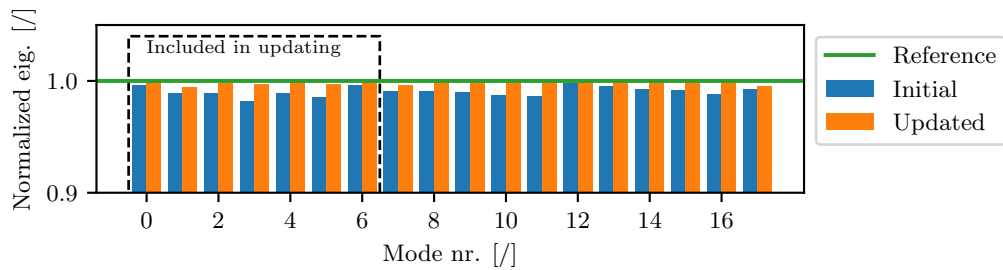


Figure 9: Comparison of the normalized eigenvalues of the initial and updated numerical model.

5. Real experiment

To validate the proposed method, a laboratory experiment was conducted. The structure under test was a 3-plane cubic shell with three orthogonal sides of $120 \text{ mm} \times 120 \text{ mm}$. The shell was manufactured by bending a 1-mm-thick metal sheet and welding the connection between two sides (see Fig. 10a). A mounting hole with a diameter of 10 mm was added in the corner of the cubic shell, where the metal sheet was bent to form a triangular flat spot with a height of 25 mm. A speckle pattern was generated using the speckle-pattern Python package [40] and was printed on a sticker and applied on the inner surface of the structure (Fig. 11).

Three single-axis accelerometers were attached to the sides at the locations indicated in Fig. 10b to monitor the structure’s response during the measurement. The structure was excited with an LDS V406 electrodynamic shaker and a PCB 208C01 force transducer was inserted between the structure and the shaker to measure the excitation force (used to normalize the response, see Sec. 2.1). The signals from the accelerometers and the force transducer were sampled using a NI-9234 acquisition card at 25 600 samples per second for a duration of 2 seconds. A random excitation signal was generated using the pyExSi [41] Python package to excite the structure up to 2000 Hz. In addition to the accelerometers, the response of the structure was measured with the Photron SA-Z high-speed camera (Fig. 12) with a sampling frequency of 20 000 Hz and a duration of 2 seconds. A chequerboard pattern was captured at different angles to calibrate the camera [42]. The shaker was rotated for each of the total of six measurements, to ensure multiple views (Fig. 13) of the structure, needed to perform the frequency-domain triangulation (see Sec. 2.1). The camera positions, based on which the triangulation was performed, are shown in Fig. 13. The displacements were identified in each view for 2637 points using the Python package pyIDI [43]. A Lucas-Kanade [44] algorithm with a subset size of 21×21 was used. The frequency-domain triangulation method (Sec. 2.1) was used to identify the 3D response and the force measurement was used to normalize the response and obtain the FRFs. The Python package pyEMA [32] was used to identify the modal shapes from the FRFs.

A 3D model of the cubic shell was designed and second-order tetrahedrons were used to construct the FE model. The model was rotated so that the triangular flat spot was parallel to the $x - y$ plane. Rigid fixation was applied in the x and y directions, but the model was not fixed in the z direction since

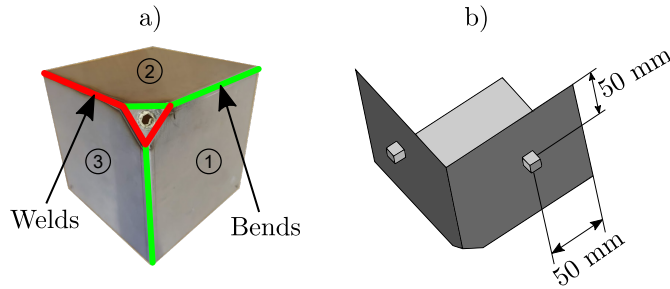


Figure 10: a) Shell manufacturing welds and bends. b) Accelerometer positions.

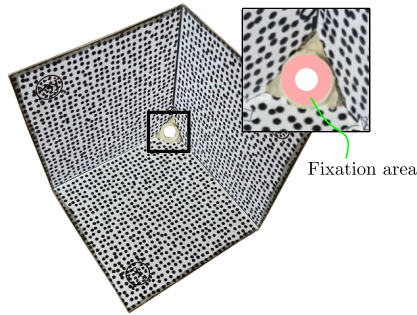


Figure 11: Speckle pattern on the structure and marked area of fixation.

the force was measured in the z direction [45]. The fixation location was an area with a radius of 18 mm, marked in the magnified part of Fig. 11. The density of the material and the Poisson's ratio were assumed to be known and were 7850 kg/m^3 and 0.3, respectively. The initial guess for the Young's modulus was 190 GPa for all elements. Each of the three accelerometers had a mass of 4 g, was modelled as a point mass and was attached to the node nearest to its true position.

The Interior Point Method was used to update the numerical model according to the algorithm presented in Sec. 3.3. Six eigenvalues and modal shapes were used in the updating procedure; therefore, the model was updated in six levels. In each level, the parameterization was performed and new parameter values were identified. The parameters identified in the sixth level were considered to be the final result.

The updated Young's moduli were computed by multiplying the identified parameters by the initial Young's moduli; the resulting moduli are presented in Fig. 14. The cubic shell is welded along the edge in the z -direction and it can be seen that the stiffness is lower along that edge. The lower Young's

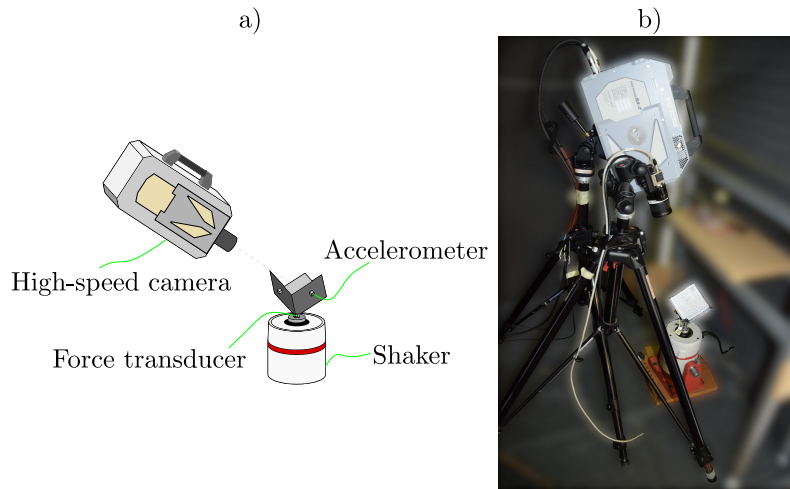


Figure 12: a) Experimental setup scheme and b) real experimental setup.

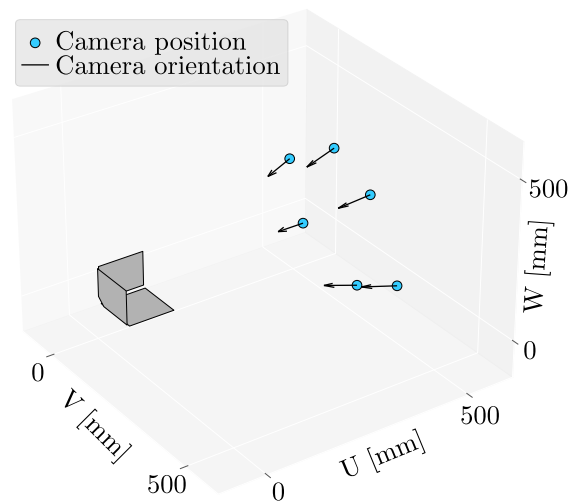


Figure 13: Camera positions identified from the images.

modulus was to be expected as a result of reduced stiffness due to a crack in the weld (part of the weld failed completely when the experiment was disassembled). Upon closer inspection, it was found that the affected area was 37 mm in length from the top edge of the cube. Additionally, a region with a higher Young's modulus in the $x - y$ plane was identified, which was not ex-

pected at that location. After an examination of the cubic shell, it was found that the side of the shell was not flat but slightly curved (an approx. 2 mm difference in height between the center and the edges), making the structure appear more stiff. The numerical model was corrected by adding a spherical curvature and the updating procedure was repeated. The parameter history

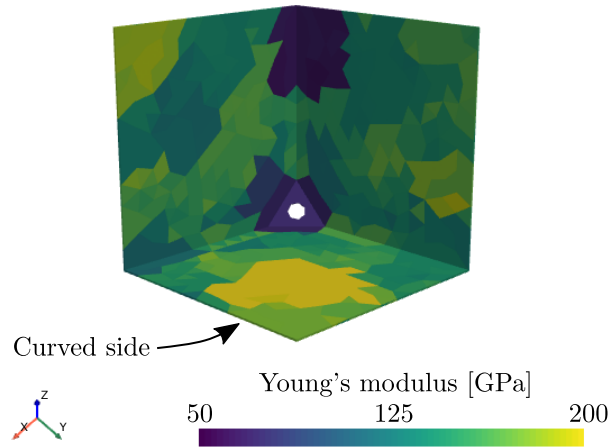


Figure 14: Identified Young's moduli for straight modeled sides.

for the first three levels is presented in Fig. 15 and the resulting Young's moduli are shown in Fig. 16. It is clear that the area with the reduced stiffness remains, while large variations of the modulus are not present in other parts of the structure. Fig. 17a shows that after updating, most eigenvalues are closer to the measured values, including the ones not included in the updating procedure; the average value of the normalized eigenvalue increased from 0.76 to 0.89. Fig. 17b shows the matching MAC values, most of which are closer to unity after the updating procedure; the average MAC value increased from 0.43 to 0.69.

6. Conclusions

A multi-level curvature-based parametrization approach was introduced in this research, enabling the parametrization of the numerical model without

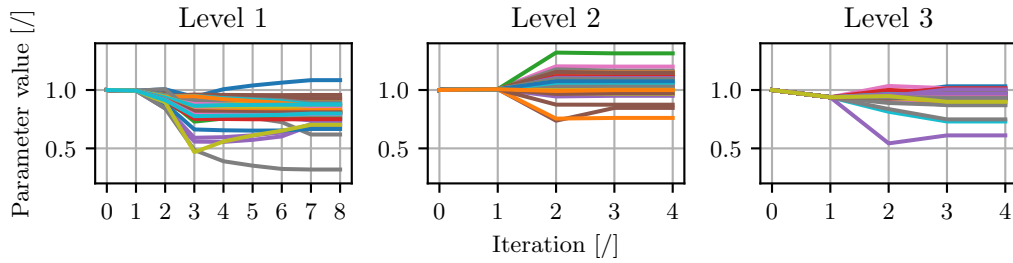


Figure 15: Parameter history for the first three levels.

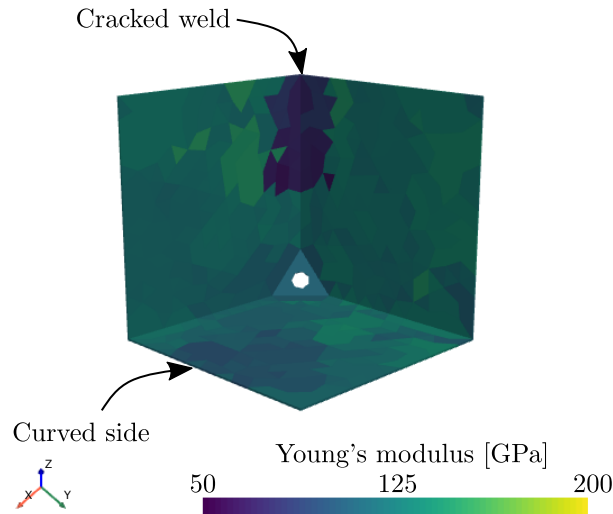


Figure 16: Identified Young's moduli of the structure with one (bottom) curved side.

pre-existing knowledge of the structure or significant engineering insight. The parameterization ensures the required sensitivity of the response to the parameters. The parameters are determined based on the curvature of each individual 3D full-field experimental modal shape and the model is updated using each parametrization consecutively. The relation between the curvature and the sensitivity was demonstrated on an Euler-Bernoulli beam and second-order tetrahedral elements. The numerical experiment was used to generate the experimental data with known parameter values. The parameters were correctly identified with the proposed method; the eigenvalues and the MAC

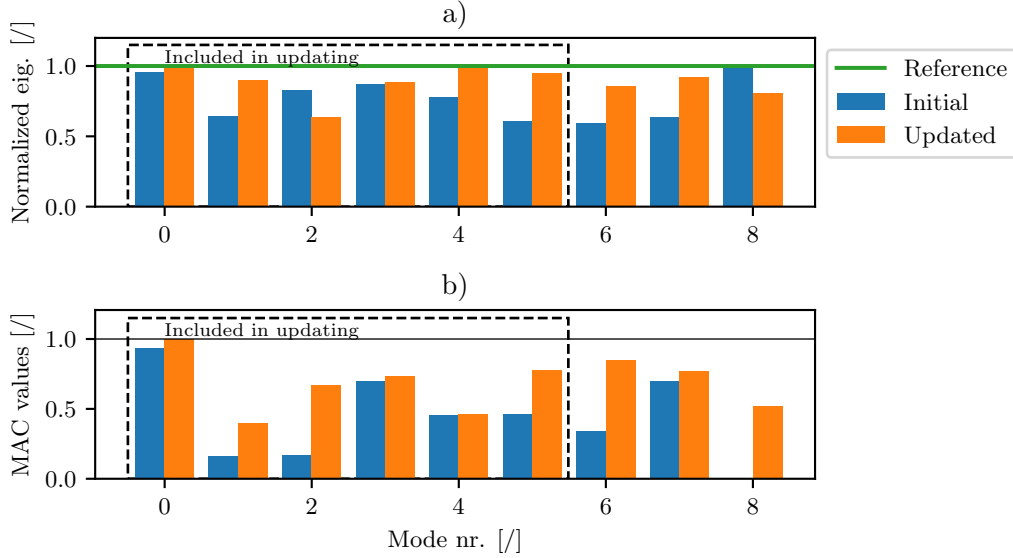


Figure 17: a) Normalized eigenvalues and b) MAC values of matching modes before and after updating.

values also showed significant improvement in the correlation between the model and experimental data.

The findings from the numerical experiment were confirmed on the real experiment, where an expected anomaly was identified (a reduced Young’s modulus in the cracked weld area). Additionally, the method identified an error in the modelling of the structure; after correcting the error, the correlation between the numerical model and the real structure increased, as indicated by the eigenvalues and the MAC values. This is also true for the modal shapes that were not included in the updating process.

It is worth mentioning that the introduced method is most suitable for shell-like structures, since the high-speed camera measures the structural response on the surface.

The proposed parametrization and model-updating method successfully identified the model parameters without significant user input. The correlation between the response of the updated numerical model and the real structure was improved and the structural anomalies were identified.

Acknowledgement

The authors acknowledge partial financial support from the Slovenian Research Agency (research core funding No. P2-0263 and research projects J2-1730 and N2-0144).

Appendix B. Modal-shape location matching

The numerical and experimental models are generally not aligned properly and do not have the same number of nodes (measurement locations). First, the models must be aligned, which was achieved by rotation and translation of the numerical model to minimize the distances between the locations on both models. The approach is known as Point Cloud Registration [46]. Second, because of the difference in the number of locations, the sizes of the modal shapes from the numerical model $\phi \in \mathbb{R}^{m_n \times l_n}$ and the experimental model $\hat{\phi} \in \mathbb{R}^{m_e \times l_e}$ were not equal ($l_n \neq l_e$) and the locations did not match. A simple comparison of closest points was found to not give the best results in the updating procedure. To enable a better direct comparison of the modal shapes, the experimental modal shapes $\hat{\phi}$ (defined at locations $\hat{\mathbf{P}} \in \mathbb{R}^{l_e \times 3}$) were approximated at the locations \mathbf{P} (locations of the numerical modal shapes ϕ). To compute the approximated experimental modal shape at location \mathbf{p}_i , denoted by ${}_{\text{ap}}\hat{\phi}_i$, c homogeneous closest neighbours $\hat{\mathbf{p}}_{ij}$, $j = 1 \dots c$, to \mathbf{p}_i were found (see Fig. A.1). The influence of $\hat{\phi}_{\hat{\mathbf{p}}_{ij}}$ on ${}_{\text{ap}}\hat{\phi}_i$ linearly decreased with the distance $\|\mathbf{p}_i - \hat{\mathbf{p}}_{ij}\|$. The inverse values of the distances between \mathbf{p} and the c closest points were therefore used as weights. The weight, $w_i \in \mathbb{R}$, of the i -th closest point $\mathbf{p}_i \in \mathbb{R}^3$ is defined as:

$$w_{ij} = \frac{1}{d_{ij}} \cdot w_{n,i}, \quad (\text{B.1})$$

where $d_{ij} \in \mathbb{R}$ is the distance between $\hat{\mathbf{p}}_{ij}$ and \mathbf{p}_i and $w_{n,i} \in \mathbb{R}$ is a normalization constant ensuring that:

$$\sum_j w_{ij} = 1 \quad (\text{B.2})$$

and is defined as:

$$w_{n,i} = \left(\sum_j \frac{1}{d_{ij}} \right)^{-1} \quad (\text{B.3})$$

To compute the value of the modal shape ${}_{\text{ap}}\hat{\phi}_i$ at location \mathbf{p}_i :

$${}_{\text{ap}}\hat{\phi}_i = \sum_j \hat{\phi}_{\hat{\mathbf{p}}_{ij}} w_{ij}, \quad (\text{B.4})$$

Since multiple closest neighbours (in this research, eight were used) were used to compute the ${}_{\text{ap}}\hat{\phi}_i$, local smoothing was implicitly applied, decreasing the noise level of ${}_{\text{ap}}\hat{\phi}_i$ (with the assumption of zero-mean normally distributed noise).

References

- [1] M. Friswell and J. E. Mottershead. *Finite element model updating in structural dynamics*, volume 38. Springer Science & Business Media, 2013.
- [2] E. Simoen, G. De Roeck, and G. Lombaert. Dealing with uncertainty in model updating for damage assessment: A review. *Mechanical Systems and Signal Processing*, 56-57:123–149, 2015.
- [3] B. T. Svendsen, Ø. W. Petersen, G. T. Frøseth, and A. Rønnquist. Finite element model updating using objective-consistent sensitivity-based parameter clustering and Bayesian regularization. *Mechanical Systems and Signal Processing*, 114:328–345, 1 2019.
- [4] D. T. Bartilson, J. Jang, and A. W. Smyth. Sensitivity-based singular value decomposition parametrization and optimal regularization in finite element model updating. *Structural Control and Health Monitoring*, 27(6):1–23, 2020.
- [5] A. Kamariotis, E. Chatzi, and D. Straub. Value of information from vibration-based structural health monitoring extracted via Bayesian model updating. *Mechanical Systems and Signal Processing*, 166:108465, 2022.
- [6] Mukesh K. Ramancha, Rodrigo Astroza, Ramin Madarshahian, and Joel P. Conte. Bayesian updating and identifiability assessment of nonlinear finite element models. *Mechanical Systems and Signal Processing*, 167:108517, March 2022.
- [7] M. Song, L. Renson, B. Moaveni, and G. Kerschen. Bayesian model updating and class selection of a wing-engine structure with nonlinear connections using nonlinear normal modes. *Mechanical Systems and Signal Processing*, 165:108337, 2022.
- [8] J. Jang and A. W. Smyth. Model updating of a full-scale FE model with nonlinear constraint equations and sensitivity-based cluster analysis for updating parameters. *Mechanical Systems and Signal Processing*, 83:337–355, 1 2017.

- [9] Richard H. Byrd, Mary E. Hribar, and Jorge Nocedal. An interior point algorithm for large-scale nonlinear programming. *SIAM Journal on Optimization*, 9(4):877–900, January 1999.
- [10] J. Nocedal and S. Wright. *Numerical optimization*. Springer Science & Business Media, 2006.
- [11] K. Zaletelj, J. Slavič, and M. Boltežar. Full-field DIC-based model updating for localized parameter identification. *Mechanical Systems and Signal Processing*, 164, 2 2022.
- [12] W. H. Peters and W. F. Ranson. Digital Imaging Techniques In Experimental Stress Analysis. *Optical Engineering*, 21(3):213427, 6 1982.
- [13] B. Pan. Digital image correlation for surface deformation measurement: historical developments, recent advances and future goals. *Measurement Science and Technology*, 29(8):82001, 2018.
- [14] Y.L. Dong and B. Pan. A review of speckle pattern fabrication and assessment for digital image correlation. *Experimental Mechanics*, 57(8):1161–1181, May 2017.
- [15] K. Zaletelj, V. Agrež, J. Slavič, R. Petkovšek, and M. Boltežar. Laser-light speckle formation for deflection-shape identification using digital image correlation. *Mechanical Systems and Signal Processing*, 161:107899, 12 2021.
- [16] Mark N. Helfrick, Christopher Niezrecki, Peter Avitabile, and Timothy Schmidt. 3d digital image correlation methods for full-field vibration measurement. *Mechanical Systems and Signal Processing*, 25(3):917–927, April 2011.
- [17] Zhilong Su, Jiyu Pan, Shuiqiang Zhang, Shen Wu, Qifeng Yu, and Dongsheng Zhang. Characterizing dynamic deformation of marine propeller blades with stroboscopic stereo digital image correlation. *Mechanical Systems and Signal Processing*, 162:108072, January 2022.
- [18] Domen Gorjup, Janko Slavič, and Miha Boltežar. Frequency domain triangulation for full-field 3d operating-deflection-shape identification. *Mechanical Systems and Signal Processing*, 133:106287, 2019.

- [19] Franck Renaud, Stefania Lo Feudo, Jean-Luc Dion, and Adrien Goeller. 3d vibrations reconstruction with only one camera. *Mechanical Systems and Signal Processing*, 162:108032, January 2022.
- [20] J. Javh, J. Slavič, and M. Boltežar. Experimental modal analysis on full-field DSLR camera footage using spectral optical flow imaging. *Journal of Sound and Vibration*, 434:213–220, 11 2018.
- [21] D. Gorjup, J. Slavič, A. Babnik, and M. Boltežar. Still-camera multi-view Spectral Optical Flow Imaging for 3D operating-deflection-shape identification. *Mechanical Systems and Signal Processing*, 152:107456, 2021.
- [22] W. Chen, D. Jana, A. Singh, M. Jin, M. Cenedese, G. Kosova, M. R. W. Brake, C. W. Schwingshackl, S. Nagarajaiah, K. J. Moore, and J. Noël. Measurement and identification of the nonlinear dynamics of a jointed structure using full-field data, Part I: Measurement of nonlinear dynamics. *Mechanical Systems and Signal Processing*, 166:108401, 2022.
- [23] M. Li, G. Feng, R. Deng, F. Gao, F. Gu, and A. D. Ball. Structural vibration mode identification from high-speed camera footages using an adaptive spatial filtering approach. *Mechanical Systems and Signal Processing*, 166:108422, 2022.
- [24] J. Javh, J. Slavič, and M. Boltežar. High frequency modal identification on noisy high-speed camera data. *Mechanical Systems and Signal Processing*, 98:344–351, 2018.
- [25] W. Wang, J. E. Mottershead, A. Ihle, T. Siebert, and S. H. Reinhard. Finite element model updating from full-field vibration measurement using digital image correlation. *Journal of Sound and Vibration*, 330(8):1599–1620, 4 2011.
- [26] A. Zanmarini. Full field optical measurements in experimental modal analysis and model updating. *Journal of Sound and Vibration*, 442:817–842, 2019.
- [27] M. Cuadrado, J. Pernas-Sánchez, J. A. Artero-Guerrero, and D. Varas. Model updating of uncertain parameters of carbon epoxy composite plates using digital image correlation for full-field vibration measurement. *Measurement*, 159:107783, 2020.

- [28] Gyeong-Ho Kim and Youn-Sik Park. An improved updating parameter selection method and finite element model update using multiobjective optimisation technique. *Mechanical Systems and Signal Processing*, 18(1):59–78, January 2004.
- [29] H. Shahverdi, C. Mares, W. Wang, and J.E. Mottershead. Clustering of parameter sensitivities: Examples from a helicopter airframe model updating exercise. *Shock and Vibration*, 16(1):75–87, 2009.
- [30] F. Nielsen. Hierarchical clustering. In *Introduction to HPC with MPI for Data Science*, pages 195–211. Springer, 2016.
- [31] Z. Fu and J. He. *Modal analysis*. Elsevier, 2001.
- [32] K. Zaletelj, B. Tomaž, D. Gorjup, and J. Slavič. ladisk/pyEMA: v0.24, 2020.
- [33] R. J. Allemang. The modal assurance criterion - Twenty years of use and abuse. *Sound and Vibration*, 37(8):14–21, 2003.
- [34] B. T. Svendsen, Ø. W. Petersen, G. T. Frøseth, and A. Rønnquist. Improved finite element model updating of a full-scale steel bridge using sensitivity analysis. *Structure and Infrastructure Engineering*, pages 1–17, 2021.
- [35] J. W. Ngan, C. C. Caprani, and Y. Bai. Full-field finite element model updating using Zernike moment descriptors for structures exhibiting localized mode shapes. *Mechanical Systems and Signal Processing*, 121:373–388, 2019.
- [36] M. Avriel. *Nonlinear programming: analysis and methods*. Courier Corporation, 2003.
- [37] O. A. Bauchau and J. I. Craig. Euler-Bernoulli beam theory. In O. A. Bauchau and J. I. Craig, editors, *Structural Analysis*, pages 173–221. Springer Netherlands, Dordrecht, 2009.
- [38] A. Gray, E. Abbena, and S. Salamon. *Modern differential geometry of curves and surfaces with Mathematica®*. Chapman and Hall/CRC, 2017.

- [39] A. Foorginejad and K. Khalili. Umbrella Curvature: A New Curvature Estimation Method for Point Clouds. *Procedia Technology*, 12:347–352, 2014.
- [40] D. Gorjup, K. Zaletelj, and J. Slavič. ladisk/speckle_pattern: v1.3.1, 2021.
- [41] A. Zorman, D. Gorjup, and J. Slavič. ladisk/pyExSi: Release of the version v0.4, 2021.
- [42] Zhengyou Zhang. A flexible new technique for camera calibration. *IEEE Transactions on pattern analysis and machine intelligence*, 22(11):1330–1334, 2000.
- [43] K. Zaletelj, D. Gorjup, and J. Slavič. ladisk/pyidi: Release of the version v0.23, 2020.
- [44] B. D. Lucas and T. Kanade. An Iterative Image Registration Technique with an Application to Stereo Vision. In *Proceedings of the 7th International Joint Conference on Artificial Intelligence - Volume 2, IJCAI'81*, pages 674–679, San Francisco, CA, USA, 1981. Morgan Kaufmann Publishers Inc.
- [45] M. Česnik, J. Slavič, P. Čermelj, and M. Boltežar. Frequency-based structural modification for the case of base excitation. *Journal of Sound and Vibration*, 332(20):5029–5039, 2013.
- [46] François Pomerleau, Francis Colas, and Roland Siegwart. A review of point cloud registration algorithms for mobile robotics. *Foundations and Trends in Robotics*, 4(1):1–104, 2015.